7-1-2003

Design and Testing of Spacecraft Power Systems Using VTB

Zhenhua Jiang
University of Miami, zjiang1@miami.edu

Shengyi Liu
Boeing, shengyi.liu@boeing.com

Roger A. Dougal
University of South Carolina - Columbia, dougal@engr.sc.edu

Publication Info

Published in *IEEE Transactions on Aerospace and Electronic Systems*, Volume 39, 2003, pages 976-989.
http://ieeexplore.ieee.org/xpl/RecentIssue.jsp?punumber=7

Design and Testing of Spacecraft Power Systems Using VTB

ZHENHUA JIANG, Student Member, IEEE
SHENGYI LIU, Senior Member, IEEE
ROGER A. DOUGAL, Senior Member, IEEE
University of South Carolina

A study is presented on the design and testing of spacecraft power systems using the virtual test bed (VTB). The interdisciplinary components such as solar array and battery systems were first modeled in native VTB format and validated by experiment data. The shunt regulator and battery charge controller were designed in Simulink according to the system requirements and imported to VTB. Two spacecraft power systems were then designed and tested together with the control systems.

Manuscript received June 6, 2002; revised November 25, 2002 and March 24, 2003; released for publication April 12, 2003.

IEEE Log No. T-AES/39/3/818504.

Refereeing of this contribution was handled by M. G. Simões.

This work was partially supported by MRJ/Veridian, under Contract 00-MRJ-1085-100, and by the NRO under Contract National Reconnaissance Office-00-C-0134. The Virtual Test Bed is developed under funding from the U.S. Office of Naval Research, under Grant N14000-00-1-0131.

Authors' address: Dept. of Electrical Engineering, University of South Carolina, Columbia, SC 29208, E-mail: (lius@engr.sc.edu).

I. INTRODUCTION

The high manufacturing cost and complexity of spacecraft electrical power systems (SEPS) make it essential to perform simulation studies and to build virtual-prototypes prior to construction of real hardware. Such prototypes help to optimize the system architecture, component choices, and the system performance in terms of efficiency, power density, cost, and lifetime. Many simulation tools have been used to study SEPS including circuit-oriented packages based on simulation program with integrated-circuit emphasis (SPICE) [1–3], general-purpose state-flow or signal-flow simulators such as MatLab/Simulink [4], or EASY5 [5–6] and application-specific softwares such as energy budget low orbit satellite (EBLOS) [7]. Each of these simulation environments favors only one model formulation method, either structural modeling (circuit schematics), or behavioral modeling (mathematical equations). The circuit oriented approach is intuitive and easy to understand, and automatically enforces the applicable conservation laws at connections between components, but in practice, it is often difficult or even impossible to model a complex system because some parts of the system do not yield to easy expression of their characteristics in terms of some limited set of existing circuit components. Therefore it is advantageous to express some models in a mathematical formulation, which is quite easy in block-diagram solvers. But block diagram solvers are generally signal flow-oriented and they do not automatically enforce energy conservation laws at connections between components. The best parts of both modeling approaches can be accomplished by using a more integrative environment such as the virtual test bed (VTB) [8–9], the philosophy of which is consistent with the IEEE standardized hardware description language VHDL-AMS [10]. VTB allows handling natural power flow, signal and data coupling between devices and offers a combination of both topological and mathematical expressions in model formulation for a comprehensive and efficient modeling process. VTB also supports multiple-layer modeling, wherein each layer can describe a different model complexity or a different behavior. In addition to the powerful capabilities for modeling, the VTB is endowed with mechanisms for both wrapping and cosimulating with models developed in other languages such as ACSL or MatLab/Simulink, and for real-time simulation with hardware-in-the-loop (HIL) [11–13]. Because of these capabilities, VTB can assist in integrating expert knowledge from many disciplines, allowing study of the dynamic behaviors of complex systems.

A typical SEPS is composed of a primary power source (solar array), an energy storage system (rechargeable batteries such as Ni-Cd, Ni-H_2,

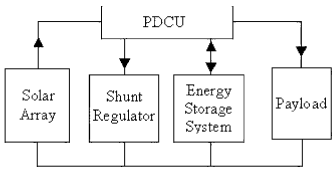

Fig. 1. Block diagram of SEPS.

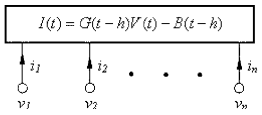

Fig. 2. Device of n terminals described by resistive companion model.

or Li-Ion, or possibly new technologies such as flywheels), voltage or current regulators, a power distribution and control unit (PDCU), and loads, as shown in Fig. 1. Complexity in modeling and simulation of such a system arises for several reasons. 1) The energy conversion and storage devices, such as solar array and battery, involve multiple-physics such as photoelectric, electro-thermal, and electrochemical processes. While conventional simulators are optimized for use within a single discipline, they are often incapable of coping with the interdisciplinary modeling in a consistent and convenient manner, and in addition to that, they have difficulties tackling strong nonlinearities existing in these devices. 2) The PDCU, responsible for power distribution, bus voltage regulation, and battery protection, contains devices for both power handling and devices for signal processing and control. The procedure that we used for design and testing of spacecraft power systems described here involved the following: models of the individual system components were developed in the native VTB format; then the control system was designed using Simulink; and finally the entire system was studied within the VTB environment by importing the Simulink models of the control elements. Using VTB, it is thus easy to build a virtual prototype of the entire system that is suitable for detailed study of the system performance, even when people from different technical areas have contributed to the definition of the various components of the system.

The remainder of this work is organized as follows. Native models for energy conversion devices such as the solar array and battery systems are described briefly in Section II. These models are also validated by experiment data. Section III describes the design and testing of the shunt regulator for the direct energy transfer system. In Section IV, the battery charging system is designed and an example spacecraft power system is assembled and tested. Both the solar array shunt regulator and the battery charge controller are implemented in Simulink and imported to VTB for system simulation. Conclusions are given in Section V.

II. COMPONENT MODELING

VTB models are independent objects that each compute their own Jacobian matrix and pass those entries into the system matrix which the network solver then solves. Natural components, those to which energy conservation principles apply, are formulated by following the resistive companion approach as described in [14]. The method starts with the mathematical expression of the device physics (or process) and yields a discretized set of time-domain equations in terms of terminal across and through variables.

The resistive companion model of an n-terminal device, as illustrated in Fig. 2, described by its across variable vector $V(t)$ and through variable vector $I(t)$, has a standard form as follows,

$$I(t) = G(t-h) \cdot V(t) - B(t-h) \tag{1}$$

where $G(t-h)$ is the device conductance matrix, $B(t-h)$ is the through-variable history vector, and

$$G(t-h) = (g_{i,j}(t-h))_{n \times n} \tag{2}$$

$$B(t-h) = -I(t-h) + G(t-2h) \cdot V(t-h) \tag{3}$$

where h is the time step size taken by the time-domain solver. The formulation of the equations is not discipline specific, so unlike structural modeling, which tends to be discipline-specific, the approach can be applied to physical processes of any discipline.

Models of two of the important energy handling devices in a spacecraft power system, the solar array and the battery, are described next.

A. Solar Array

The process of converting solar energy into electric energy in a semiconductor solar cell is well known [15–19]. Heat is also generated due to direct absorption of photons that do not create electric power and also by ohmic losses. Since the energy conversion process is affected not only by the cell properties and the load condition, but also by the solar irradiance and the temperature, it is necessary to build a multiphysics model [20] involving three energy domains: light, electricity and heat. There are four terminals in the model based on consideration of its interactions with its surroundings. The terminals v_0 and v_1, denoted by their across variables (voltages in V), are electrical in nature and deliver electric energy to the load. The terminal v_2 (or P, the solar irradiance on the cell surface in W/m^2) is a light-receiving terminal, which is a signal terminal in the model. And the terminal v_3 (or T, the temperature of the cell in K) is thermal in nature and it conducts heat power to the ambient.

The electrical characteristic of a solar cell can be mathematically expressed as,

$$i(t) = \frac{1}{R_s}\left(v(t) - \gamma v_{th}(t)\ln\left(\frac{I_P(t) + i(t) - \dfrac{v(t)}{R_{sh}}}{I_{sat}(t)} + 1\right)\right) + \frac{v(t)}{R_{sh}} \tag{4}$$

where v and i are the voltage (V) and current (A) at the solar cell terminals, γ is the cell diode ideality factor, and R_s and R_{sh} are the cell body series and shunt resistances (Ω). The thermal potential v_{th} (V), saturation current I_{sat} (A), and the diode current i_d (A) can be expressed, respectively, as

$$v_{th}(t) = \frac{kT(t)}{e} \tag{5}$$

$$I_{sat}(t) = I_{sat0}\left(\frac{T(t)}{T_0}\right)^3 \exp\left(\frac{e}{\gamma k}\left(\frac{E_g(T_0)}{T_0} - \frac{E_g(T(t))}{T(t)}\right)\right) \tag{6}$$

$$i_d(t) = I_{sat}(t)\left(\exp\left(\frac{v_d(t)}{\gamma v_{th}(t)}\right) - 1\right) \tag{7}$$

where k and e are Boltzmann constant and the electronic charge, respectively, T_0 the reference temperature (K), T the cell temperature (K), I_{sat0} the saturation current at the reference temperature (A), E_g the energy band gap (eV), and v_d the diode voltage (V). The light-induced current (A), which is given in (8), is directly proportional to the irradiance

$$I_P(t) = \Re AP(t) + C[T(t) - T_0]\frac{P(t)}{P_0} \tag{8}$$

where A is the cell active area (m^2), C is the temperature coefficient of light-induced current (A/K), P is the irradiance (A/m^2), P_0 is the irradiance at the temperature T_0 (A/m^2), and $\Re$ is the spectral-averaged responsivity (A/W).

The heat transported through the thermal terminal is characterized by the energy balance equation, as given by following equation [20]

$$c_p M\frac{dT(t)}{dt} = \frac{[v(t) - v_d(t)]^2}{R_s} + \frac{[v(t)]^2}{R_{sh}} + i_d(t)v_d(t) + (1 - \rho - \tau - \eta)AP(t) + Q \tag{9}$$

where c_p is the averaged specific heat (J/kg/K), M is the averaged mass (kg), the symbols ρ, τ, and η denote the reflection coefficient, transmission coefficient, and quantum efficiency of the cell, Q is the heat power changed with the connected component (W). Equation (9) explains that the energy absorbed by the cell (resulting in temperature increase) is due to the heating by electro-thermal processes (the first three terms on the right-hand side), direct absorption (the fourth term), and heat exchange with connected structures (the last term).

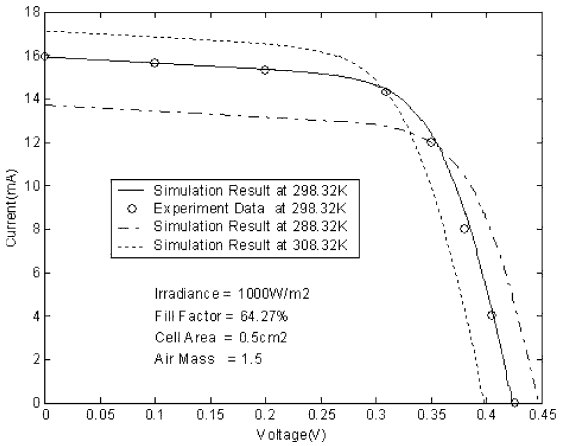

Fig. 3. Comparison of simulated and experimental i-v characteristics.

The standard equations as shown in (1)–(3) can then be derived for solar array model based on (4)–(9). Note that this model is a general model based on the physics of solar array. A specific solar array can be modeled by changing the model parameters. In order to validate this model, the simulated i-v characteristic for a particular solar cell is compared with experiment data. The experiment was performed for a 0.5 cm^2 copper indium diselenide ($CuInSe_2$) thin film solar cell [19] at an irradiance of 1000 W/m^2 and at 25°C [21]. The air mass is 1.5 and fill factor the solar cell is 64.27%. The measured i-v characteristic is given in Fig. 3. Also plotted in Fig. 3 are the simulated i-v curves at 15°C, 25°C, and 35°C, respectively. The same irradiance and solar cell parameters are used in the simulation. From Fig. 3 it is clear that the simulation result agrees well with the experiment data at 25°C. It is also seen that the open circuit voltage decreases with the temperature while the short circuit current increases with the temperature.

B. Battery System

Energies in battery systems are of chemical, electrical, and thermal forms. Internally, the battery converts chemical energy into electrical energy during discharge (or the reverse during charge), and it generates heat due to both irreversible processes (e.g. ohmic heating) and reversible processes (entropy change). Externally, the battery interacts with its surroundings both electrically (delivering electric power via the electrical terminals) and thermally (transporting heat through its surface).

Several detailed Ni-H_2 battery models have been published, among which the model of Wu, White, and Weidner et al. [22–24] includes considerable details of the electrochemical kinetics and thermodynamics.

VTB allows capture of their expertise in the electrochemical discipline by integrating their battery model into the VTB environment. The Ni-H_2 battery model presented here results from collaboration with these authors. The present model is somewhat simplified, but it still captures the major features of Ni-H_2 characteristics. Two reactions are considered: the nickel reduction/oxidation at the positive electrode, which is a decisive reaction for the battery potentials, and the water oxidation (or oxygen evolution), which dominates the over-charge process. Hydrogen reaction at the platinum electrode, intermediate reactions, and side reactions are ignored. In addition, the kinetics of chemical reactions are assumed to be fast enough as to not limit the current response.

The overall reversible potential, $E_{\mathrm{Ni}}(T,x)$, corresponding to the nickel reaction, and the resulting current from the oxygen reaction, $i_{\mathrm{O}_2}(T)$, are determined by (10) and (11)

$$E_{\mathrm{Ni}}(T,x) = E^0_{\mathrm{Ni}}(T) + \frac{RT}{F}\ln\left(\frac{1-x}{x}\right) + \frac{RT}{2F}[A_0(T)C(x) + B_0(T)D(x)] \tag{10}$$

$$i_{\mathrm{O}_2}(v,T) = AL_+ ai_{0,\mathrm{O}_2}(T)\exp\left[4(1-\alpha_{\mathrm{O}_2})\frac{F}{RT}(v - E_{\mathrm{O}_2}(T))\right] \tag{11}$$

where R is the gas constant (8.314 J/mol/K), F is the Faraday constant (96,485 coulombs/mol), x and T are state of discharge and temperature of the battery, both of which are functions of time, E^0_{Ni}, A_0, and B_0 are functions of temperature only, and C and D are functions of the state of discharge only, A and L_+ are the electrode area and thickness, respectively, α_{O_2} is the transfer coefficient for oxygen reaction, v is the battery terminal voltage (V), E_{O_2} is the reaction potential (V), a is the specific area ($\mathrm{m}^2/\mathrm{m}^3$) of the electrode, and $i_{\mathrm{O}_2,0}$ is the exchange current density ($\mathrm{A/m}^2$).

The state of discharge, at any time instant t, is determined by the available active material in the battery. The change rate of the state of discharge is conveniently related to the nickel reaction current i_{Ni} as,

$$\frac{dx}{dt} = -\frac{i_{\mathrm{Ni}}}{Q_{\max}} \tag{12}$$

where $Q_{\max}$ is the maximum charge stored in the battery for a given capacity (C). In addition, the battery terminal voltage can be related to the current, considering internal potential losses, as,

$$v = E_{\mathrm{Ni}} + R_i \cdot i_{\mathrm{Ni}} \tag{13}$$

where R_i (Ω) is a fitting parameter representing overall internal resistance due to ohmic, surface kinetic, and concentration limitation losses.

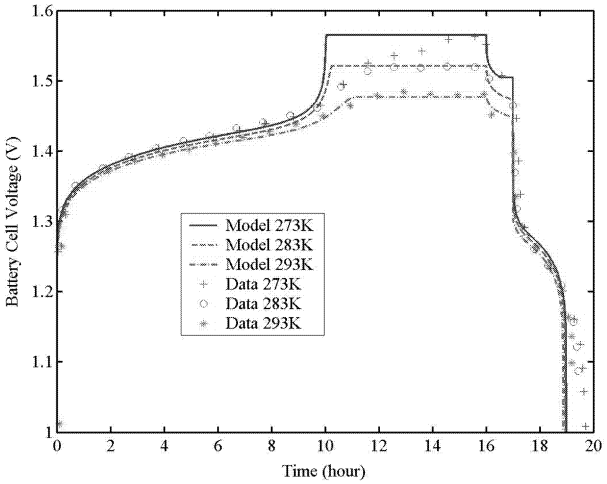

Fig. 4. Battery cell voltages in cycle of charge-overcharge-self discharge-discharge at 3 ambient temperatures.

The heat energy in the battery is characterized by the energy balance equation given in (14)

$$c_p m\frac{dT}{dt} = i_{\mathrm{Ni}}\left(v - E_{\mathrm{Ni}} + T\frac{\partial E_{\mathrm{Ni}}}{\partial T}\right) + i_{\mathrm{O}_2}\left(v - E_{\mathrm{O}_2} + T\frac{\partial E_{\mathrm{O}_2}}{\partial T}\right) + Q_b \tag{14}$$

where m is the battery mass (kg), c_p is the average specific heat (J/kg/K). Notice that heat terms include both reversible and irreversible (resistive) ones, Q_b is the heat transported to the surroundings due to cooling mechanisms.

The battery cell voltage profiles in a cycle of charge, overcharge, self-discharge, and discharge are shown in Fig. 4 and compared against the TRW 30 Ah module data [23]. As can be seen, the model fits the experimental data very well for the normal charging (first 10 h) at all three temperatures. The model also has a good agreement with the data for self discharge and discharge processes above 1.15 V (16–19 h). During the overcharge processes, the model yields constant voltages that sharply distinct the normal charge and overcharge regions, while the experimental data show slow ramps before reaching ultimate overcharge voltage. One of the possible reasons for the discrepancy may be due to strong nonlinear overpotentials resulting from various mechanisms in the overcharge process, which are not included in the model. Notice that the ultimate overcharge voltages from the model, which are 1.544 V, 1.5 V, and 1.46 V, are very close to those of the experimental data, which are 1.58 V, 1.52 V, and 1.48 V, for the temperatures of 273 K, 283 K, and 293 K, respectively. This fact will allow the model to still serve the purpose for battery overcharge control by setting an appropriate cutoff pressure. The behaviors of the battery voltage under the effect of temperatures are consistent with the experimental

data over the entire cycle. That is, lower temperatures yield higher voltages and also longer discharge life, suggesting that the battery is preferably operated at low temperature for high-power efficiency. The significant discrepancy between the model and the data is seen when discharging below 1.15 V, where the experimental data show larger discharge capacity, and the temperature effect is more pronounced. This may be due to the fact that the appearance of γ-phase of nickel oxyhydroxide contributes to the discharge capacity [23]. Although the model does not account for the discharge behavior below 1.15 V, it can be concluded that the model matches the experimental data very well within the normal operation range.

More details of the Ni-H_2 battery model can be found in [25]. Furthermore, a dynamic lithium ion battery model suitable for VTB simulation is presented and validated in [26].

C. Other Components

The irradiance model computes the illumination of the solar array based on the date/time and the orbital parameters of the spacecraft. The user can select between low Earth orbit and geo-synchronous orbit. The model can output Earth position, Earth rotation, and the position of the spacecraft for use in the visualization system. Heat carried away through the radiator follows the blackbody radiation law.

Also included in the studied systems are models for conventional components such as a buck converter, current sensor, resistor, capacitor, and diode, which are not described in detail here.

III. SHUNT SYSTEM DESIGN AND TESTING

Shunt regulators are used in SEPS to limit the power bus voltage by dissipating the excess solar array power. They can be implemented in many ways, such as sequential shunt system, partial shunt system, digital shunt system, etc. [27–30]. A sequential shunt regulation system is designed here as an example, in which each shunt can be implemented either by a metal-oxide semiconductor field-effect transistor (MOSFET) switch in series with a shunt resistor, or by a MOSFET driven bipolar junction transistor (BJT) pair where the BJT pair acts as the dissipative element, or other combinations. Here we use the former implementation, which is modeled as an ideal switch in series with a dissipative resistor.

The objective of the sequential shunt regulator is to switch in or out solar array sections sequentially in order to select the number of solar array sections needed to both supply the load and to charge the batteries in a desired manner. According to this requirement, a sequential shunt regulator for four solar array sections is designed in Simulink, as shown in Fig. 5. The shunt regulator model produces four

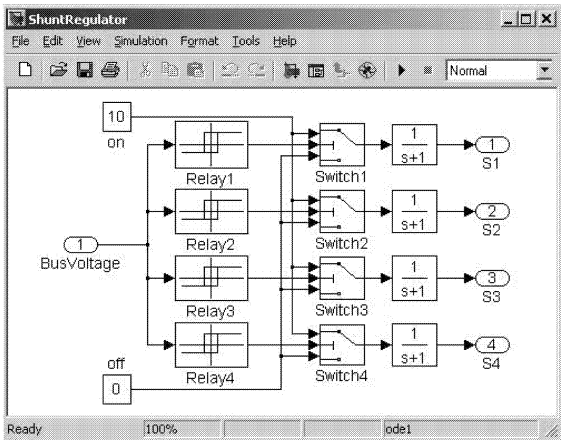

Fig. 5. Simulink model of proposed sequential shunt regulator.

switching signals, $S1$, $S2$, $S3$, and $S4$, for the shunt elements by comparing the bus voltage with the four pairs of upper and lower voltage setpoints, which are user defined. When the bus voltage exceeds an upper limit, the corresponding switching signal is on and the solar array section is shunted. When the bus voltage drops below the lower limit, an off switching signal is produced to deactivate the corresponding shunt element. This Simulink model can be used in either of two ways. First, when the controller is still in development, the Simulink model can be used in an interactive cosimulation mode that allows adjustment of the controller parameters during system simulation. Second, once the controller design has been finalized, the controller model can be compiled into an executable that allows others to study the system behavior without having to actually run Matlab or Simulink.

While the shunt regulator on the solar array provides an appropriate bus voltage to the battery as a whole, additional regulators are needed across individual cells of the series-connected battery to prevent mismatch in the state of charge which may occur due to minor differences among the cells. These regulators were implemented as voltage-controlled switches with hysteresis. When the battery voltage exceeds a preset level, the resistor is connected in parallel to the battery terminals. The battery discharges through the shunt resistor and the voltage decreases. When the battery voltage drops below another predetermined value (or reactivation voltage), the shunt branch is disconnected.

Next, we investigated the operation and any interactions between the sequential solar array shunt regulator and the individual battery shunt regulators, by studying the direct energy transfer (DET) power system shown in Fig. 6. This system was assembled by dragging the models from the model library, putting them in the schematic view and connecting them properly. In Fig. 6, four solar array strings: $SA1$–$SA4$, are sequentially shunted array sections,

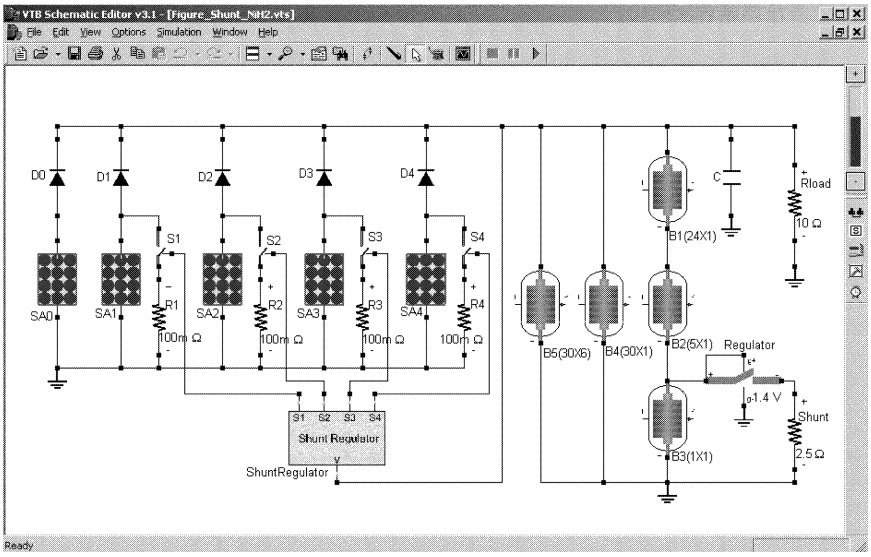

Fig. 6. Schematic diagram of simplified DET SEPS.

which perform coarse regulation of the bus voltage. An active array section, $SA0$ is directly connected to the main bus without shunt. Each section is individually switched in or out depending on the bus voltage and the switching reference voltages except the active section which is connected to the bus all the time. Here a 2-terminal solar array model is used for the simplification of the system since VTB supports multiple-layer modeling. The illumination and thermal characteristics are incorporated directly in this particular version of the solar array model. A sequential shunt regulator controls the switching of the four shunt elements. It is compiled from Simulink model and imported to VTB. The upper voltage setpoints of the regulator for solar array sections $SA1$–$SA4$ are 41.50 V, 41.48 V, 41.45 V, and 41.40 V, respectively. The lower setpoints are 41.4 V, 41.2 V, 41.1 V, and 41.0 V, respectively.

Each solar array section is an 88×2 array of cells (in series by parallel connections). The Ni-H_2 battery is nominally an array of 30×8 cells, but in the simulation model two individual series strings are split out for more detailed study, and in one of those strings, an individual cell is revealed. Accordingly, the numbers of series and parallel cells are (24×1), (5×1), (1×1), (30×1), (30×6), respectively, for $B1$–$B5$. The initial state of charge of $B3$ cell is 0.70 while those of all the others are 0.60. The load is a resistor of 10 Ω. A filter capacitor connected to the main bus is used to smooth the bus voltage. The resistance of the shunt resistor for a solar array section is chosen as 0.1 Ω, and then a shunt element that can bear more than 10 W ohmic heat is needed since the short-circuit current of a solar array section is about 9.5 A. To prevent an individual battery cell from overcharging, the turn-on voltage of the battery shunt is set to 1.4 V and the reactivated voltage is 1.38 V. The resistance of the shunt element is chosen as 2.5 Ω, through which about 550 mA current will conduct when the battery is shunted. In this case, power of about 0.8 W is dissipated in each battery shunt. For convenience, only one battery shunt is shown in Fig. 6.

Simulation is conducted for the first 40 min of the orbit cycle to test the performance of the shunt system. The simulation results are given in Figs. 7–10. Fig. 7 shows the output currents from four shunted solar array sections, which contribute to load requirement and battery charging. Note that each of them is not the actual current through the solar array, but the current through the blocking diode or the current that is not shunted. Fig. 8 shows the bus voltage which increases initially from 40.0 V. From Figs. 7 and 8, it can be seen that when the bus voltage arrives at the 41.40 V setpoint of the shunt regulator, solar array $SA4$ is first shunted, and the output current from this section becomes zero. Then the remaining four solar array sections, including the active section, provide power for the batteries and load. There is a rapid but small decrease in amplitude of the bus voltage and afterwards the bus voltage increases. The solar arrays $SA3$, $SA2$, and $SA1$ are sequentially shunted when the bus voltage arrives at their setpoints. After four sections are shunted, the bus voltage will decrease continuously because the active section cannot support the load and the batteries begin to discharge. When the bus voltage decreases below 41.4 V, section $SA1$ is activated again.

Due to the differences in initial states of charge of the batteries, the battery cell voltages are different. The voltage of battery cell $B3$ increases faster than the others and it arrives at the upper limit setpoint first, which is shown in Fig. 9. From Fig. 9, it is clear that when the voltage of cell $B3$ exceeds 1.4 V, the

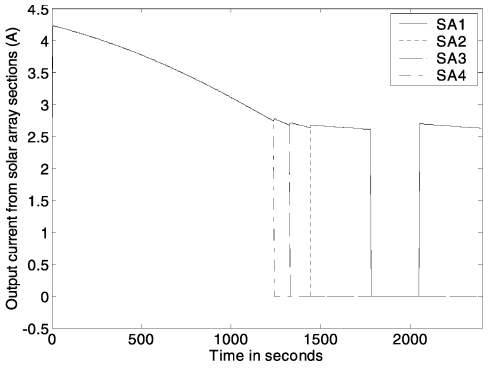

Fig. 7. Output currents from four solar array sections: SA1 (line), SA2 (dot), SA3 (dash), and SA4 (dash-dot).

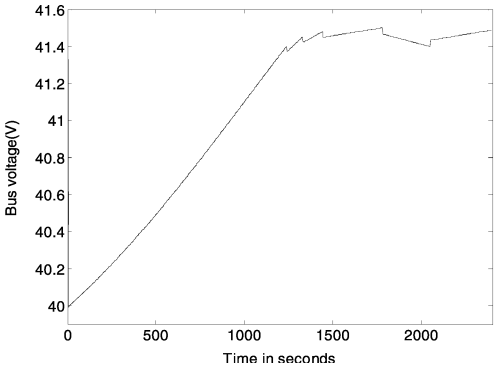

Fig. 8. Simulation result of bus voltage.

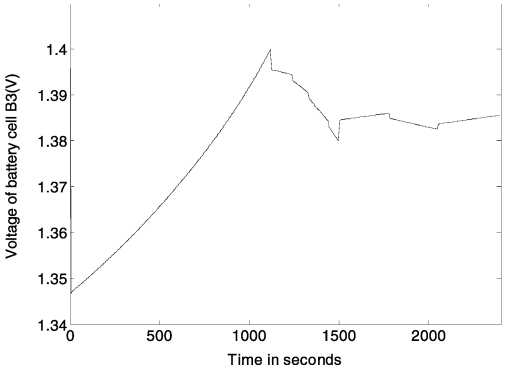

Fig. 9. Voltage of battery cell B3.

shunt is activated. Then this battery discharges and the voltage decreases. When the battery voltage drops below 1.38 V, the shunt is deactivated and the battery is charged again. The difference of the states of charge of batteries $B2$, $B3$, and $B5$ is shown in Fig. 10. The state of charge of $B3$ is the highest, and the other two are close. From Fig. 10, it is seen that the state of charge of $B3$ begins to decrease at about 1100 s because it is shunted. From the simulation results, it can be seen that the sequential shunt regulator can maintain the bus voltage at a relatively constant level and battery shunt contributes to charge equalization.

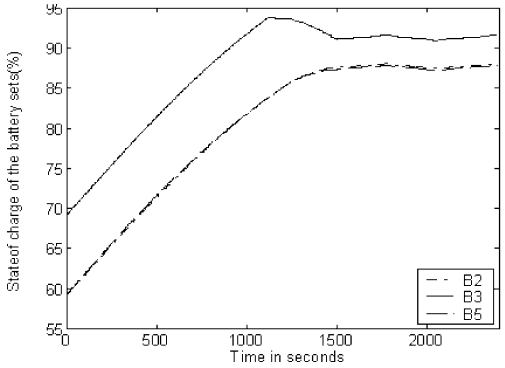

Fig. 10. States of charge of three battery sets: B2 (dash), B3 (line), and B5 (dash-dot).

IV. BATTERY SYSTEM DESIGN AND TESTING

In a spacecraft power system, the battery is used to store the energy when the solar array is illuminated and to provide power for the loads during eclipse. An important criterion for the system design is that the capacity of the battery should meet all load power demands during eclipse. The lithium ion batteries are not yet widely used in spacecraft systems but are attractive due to their high capacity, light weight, and long life. However, when charging Li-Ion cells, it is hazardous to exceed certain current or voltage limits. Therefore, the charging operation should be regulated appropriately. Another design criterion is then that the battery charger should produce an accurately regulated charging current and voltage.

Here we studied a 100 W system which operates in low Earth orbit, with a nominal solar array voltage of about 50 V. The payload is represented as a combination of a resistive load, which is connected to the 28 V regulated bus, and a pulsed power load, which is connected directly to the unregulated voltage bus and in which a regulator is incorporated. In order to sustain the bus voltage during eclipse, 10 lithium ion cells are connected in series, each having a capacity of 1.5 Ah. Taking into consideration the load power demand during eclipse, 3 such battery strings are connected in parallel. The battery is charged by a buck converter controlled by a battery charge/discharge controller by dynamically monitoring the voltage, current, and temperature of the battery. The charge controller follows a regimen consisting of constant current during charging followed by a constant voltage float. The reference voltage is temperature compensated. Both current and voltage regulators employ the classical proportional-integral control strategy. The control scheme can be described as follows

$$V_{\text{ref}} = V_{\text{ref0}} - C_T(T - 293.32) \tag{15}$$

$$d = d_{\text{old}} + k_{pi}(I_{\text{ref}} - I) + k_{ii}\int (I_{\text{ref}} - I)dt, \quad \text{if} \quad V < 0.98 \times V_{\text{ref}} \tag{16}$$

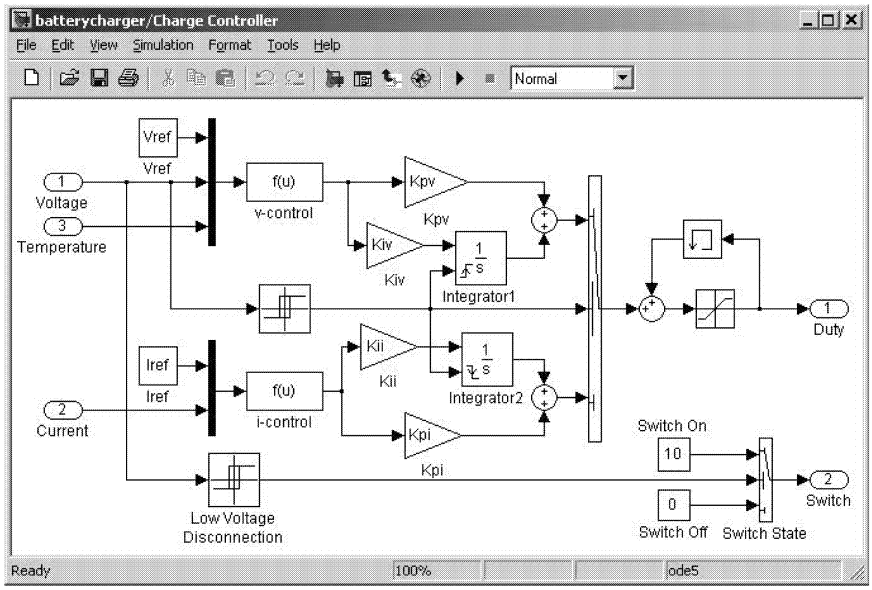

Fig. 11. Simulink model of proposed battery/discharge controller.

$$d = d_{\text{old}} + k_{pv}(V_{\text{ref}} - V) + k_{iv}\int (V_{\text{ref}} - V)dt,$$

$$\text{if} \quad V \geq 0.98 \times V_{\text{ref}} \qquad (17)$$

where V, I, T are the sampled voltage, current, and temperature of the battery, respectively, d and d_{old} are the current and previous duty ratios used to control the buck converter, V_{ref0} and I_{ref} are the desired voltage and charging current of the battery at 293.32 K, C_T is the temperature coefficient with respect to the voltage, k_{pi}, k_{ii}, and k_{pv}, k_{iv} are the proportional and integral gains for current and voltage regulations, respectively.

The battery charge/discharge controller was designed in Simulink as shown in Fig. 11. Three input terminals are for the sampled voltage, current, and temperature of the battery, respectively. The output duty ratio is obtained from either the voltage-control loop or the current-control loop, depending on the battery voltage. An output memory mechanism guarantees a smooth change between these two control schemes. The switch signal terminal is used to manage discharging of the battery. When the monitoring voltage is below a preset value (or low voltage disconnection setpoint), the controller can output a signal to disconnect the loads in order to protect the battery from overdischarging. A hysteresis allows reconnecting the loads when the battery voltage increases to an acceptable level.

The studied system, assembled in VTB, is shown in Fig. 12. It comprises a solar irradiance model to illuminate the solar cells, a solar array to convert the solar illumination into electrical power, a lithium ion battery array, a resistive load, and a pulsed power load. Several auxiliary components in the system are responsible for appropriate and efficient operation of the entire system. The primary energy conversion device is an 88×10 (series by parallel connections) array of single junction silicon cells. Each cell has an active area of 2.4×6.6 cm^2, and a responsivity of 0.35 A/W. The battery is a 10×3 array of Li-Ion cells, each having a nominal voltage of 4.15 V and a capacity of 1.5 A-hrs. The initial state of charge of the battery is 0.6. All the solar array cells and all the battery cells are lumped into a single model for this particular orbital simulation. Shunts for solar arrays are not included in this system. The charge controller is compiled from the Simulink model and imported to VTB. The pulsed power load consists of a 55 W constant power load and a 5 W pulse power load which is active once every second. Another load is a 20 Ω resistive load which is connected to a 28 V regulated voltage bus. The charging current reference and floating voltage reference for the battery charge controller are 3 A and 41.5 V, respectively.

This system is simulated for the first 14 ks of the mission, and the calculated results for this system are shown in Figs. 13–18. The time axis in these figures is scaled in seconds and the time step for simulation is 100 ms. Fig. 13 shows the power profiles of the solar array, Li-Ion battery, and loads. As can be seen, when the solar array is in light, it provides power for the loads, charging the battery simultaneously. The power from the solar array is the sum of the load power and the power to the battery. During eclipse, the battery provides power for the loads, and the bus voltage decreases from a value approximately equal to solar array voltage to the battery voltage, which is shown in Fig. 16. The power dissipated by the resistive load does not change with the bus voltage since its voltage is regulated. After a cycle, the solar array powers the loads and charges the battery again.

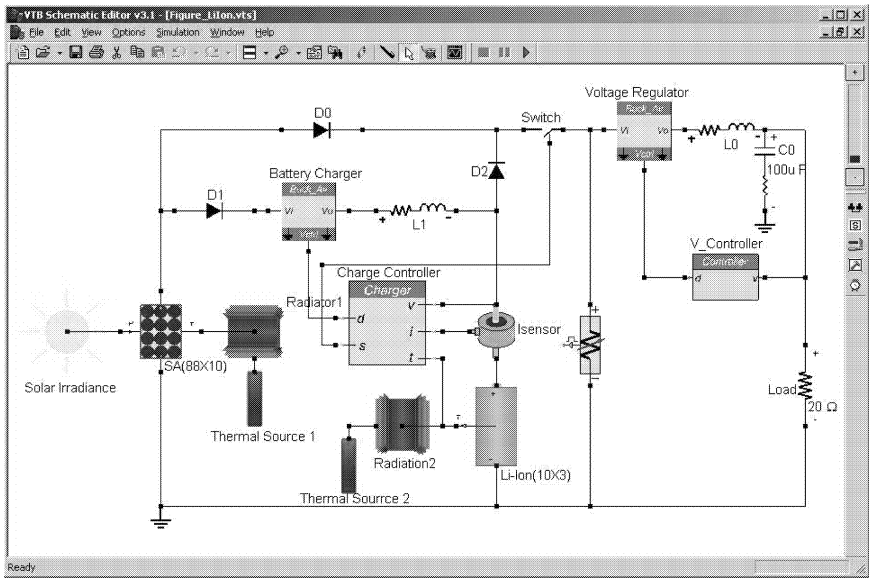

Fig. 12. Schematic view of example SEPS.

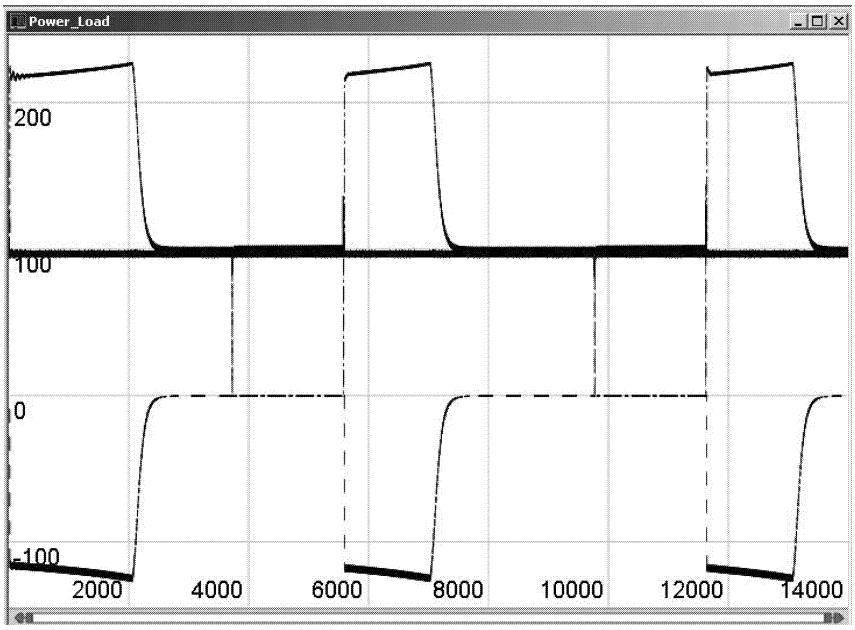

Fig. 13. Power profiles of solar array (dash-dot), Li-Ion battery (dash), and loads (solid line).

Figs. 14 and 15, respectively, show the sampled data for the voltage and current of the lithium ion battery. The battery is initially charged at 3 A current, and the charge current has small ripples due to the pulsed power load. After about 2000 s of constant current charging the battery voltage arrives at the preset point and thereafter it floats at that voltage. Actually the voltage reference is a little higher than 41.5 V because the battery temperature at this time is lower than the reference value that is set on the ground. When the charging operation moves to constant voltage mode, the charging current tapers immediately. When the solar array goes into eclipse, the battery begins to discharge. As a result, the battery current reverses and its voltage decreases. The discharge current is not controlled and depends on the loads. It is seen from Fig. 15 that the discharging current is about 2.3 A. At the end of the discharge cycle, the battery voltage decreases to about 38.7 V. It is clear from these two figures that the charge controller performs the constant current charging/constant voltage floating scheme correctly.

Fig. 17 illustrates the calculated state of charge of the battery, which increases initially from 0.6 and approaches to 1.0 when it is fully charged. The state of charge decreases to 0.7 at the end of discharging. After several cycles, the state of charge fluctuates between 0.7 and 1.0. From this figure, it is seen

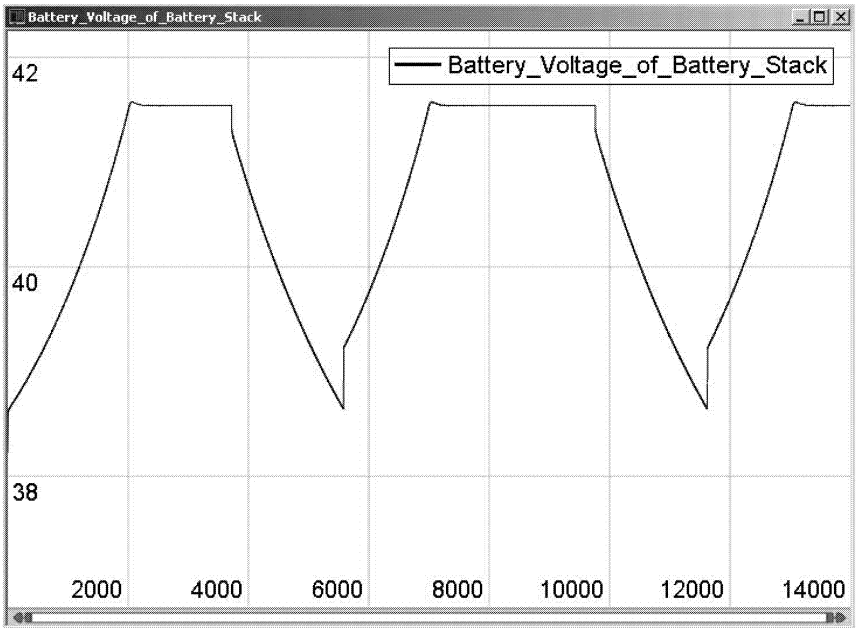

Fig. 14. Li-Ion battery voltage. Battery voltage increases from 38.7 V. After about 2000 s of 3 A charging it arrives at preset point and thereafter floats at that value. Voltage decreases to about 38.7 V during the discharge cycle.

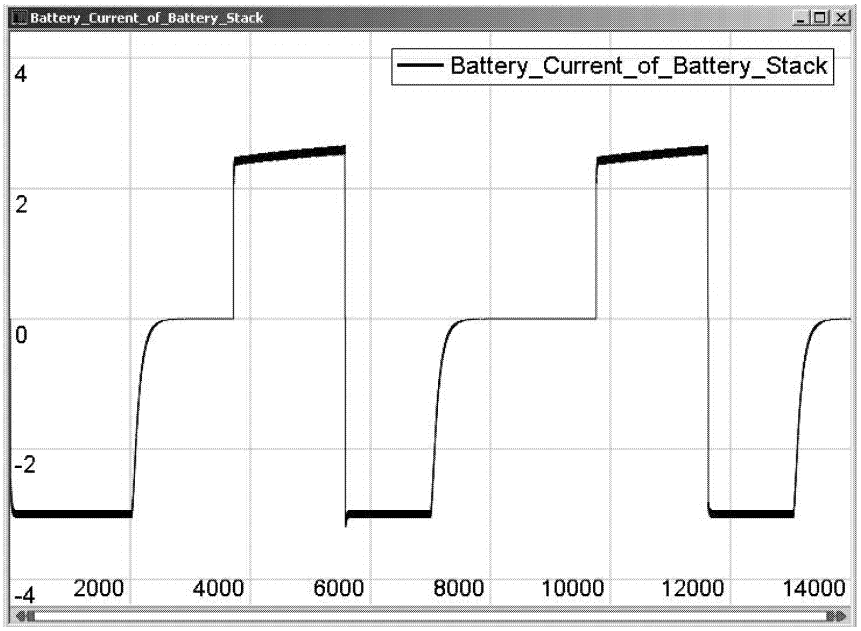

Fig. 15. Li-Ion battery current. Battery is initially charged at 3 A current. After battery voltage arrives at reference value, battery current tapers immediately. Discharge current is about 2.3 A.

that the capacity of the chosen battery meets the load power requirement. Fig. 18 gives the energy conversion efficiency of the solar array, which is about 12% when it powers the battery and loads simultaneously. The efficiency declines as the output current decreases because the output power decreases.

Temperature control in a spacecraft power system is an important consideration. If the battery becomes too cold, its ability to accept or supply power is reduced [31]. If the temperature rises too high, irreversible electrolyte and electrode decomposition can occur. Battery power can be used to run a resistive heater to keep the battery warm, but that then requires a larger battery because the battery has to power both the electronic loads and the heater. Alternatively, the battery capacity can be increased so that it still has sufficient capacity at low temperatures. These two competing approaches can be traded off by using a tool such as the VTB that supports full evaluation of the thermal effects. In the study described previously, the battery was sized according to the load power demand at a standard temperature. But the battery size

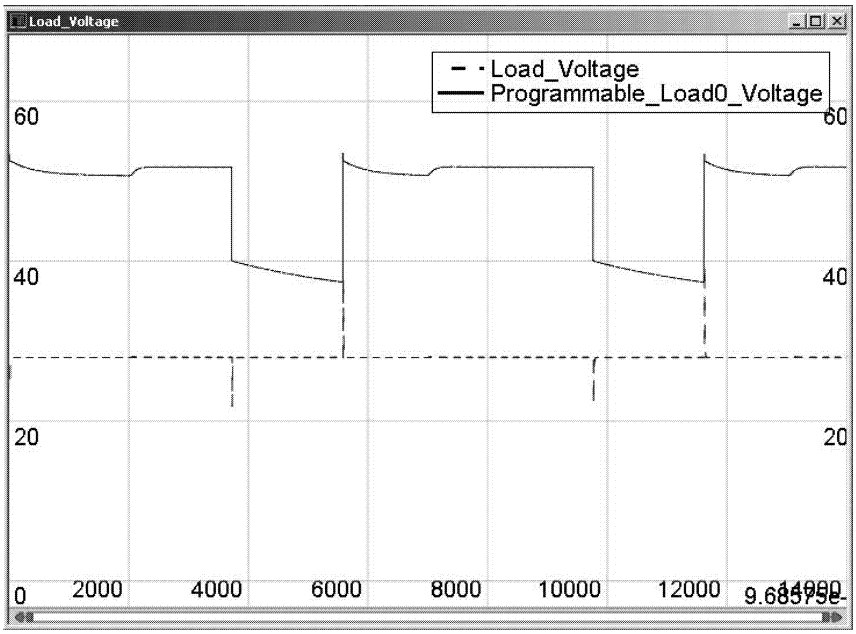

Fig. 16. Regulated and unregulated bus voltages.

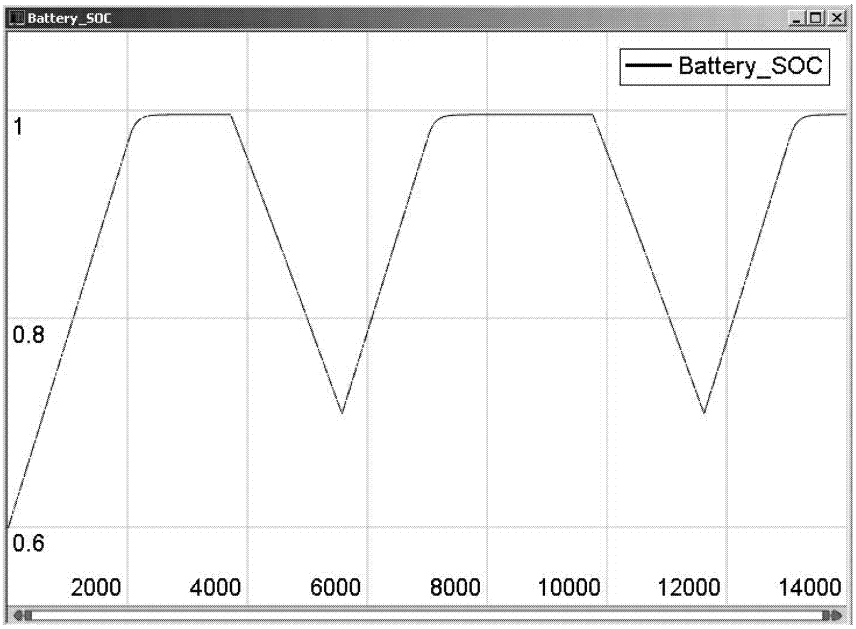

Fig. 17. State of charge of Li-Ion battery.

could now be refined by taking into account the effect of the temperature fluctuations on the power that the battery can store or supply.

V. CONCLUSIONS

Interdisciplinary models such as solar array and battery systems were developed natively in VTB and validated by experiment data. Based on these validated models, a DET system and a representative SEPS were designed according to specific criteria. The control systems such as shunt regulator and battery charge/discharge controller were designed and implemented in Simulink according to the system requirements and then imported into the VTB for system simulation.

The DET system was tested together with the shunt regulators, and the details of the operation and performance of the sequential shunt regulator and battery shunt were studied. The sequential shunt regulator correctly selected the number of solar array sections needed for both supplying the load and charging the batteries and it switched in or out solar array sections sequentially. The shunt regulator maintained the bus voltage at a relatively constant level. The battery shunt properly equalized

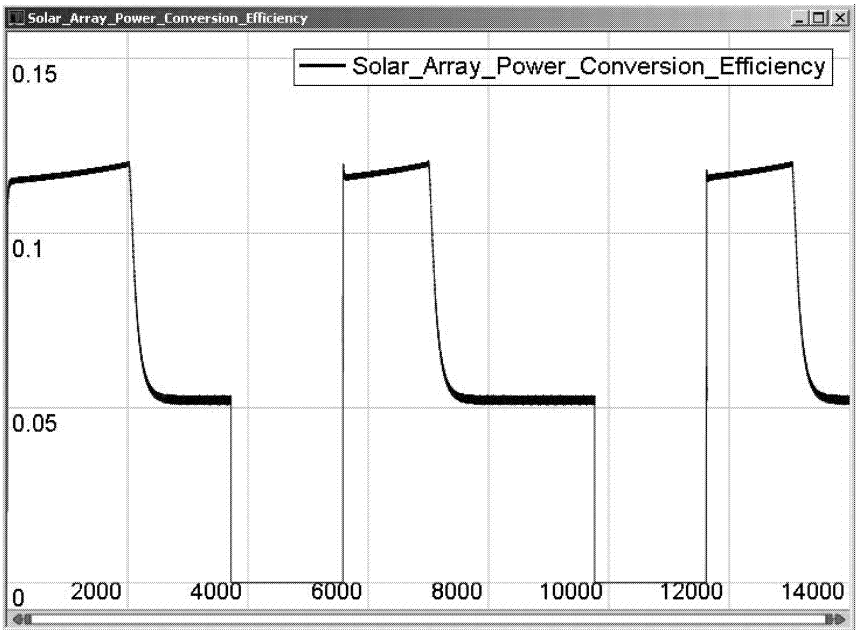

Fig. 18. Energy conversion efficiency of solar array.

the charge of intentionally mismatched battery cells. The representative spacecraft power system was tested for a couple of orbital cycles. The behaviors of the solar array and battery were studied in details. It can be seen from the simulation results that the proposed system configuration and parameters met the system requirements and that the proposed battery charge controller correctly performed the constant current/constant voltage strategy.

REFERENCES

[1] Nelms, R. M., Evans, B. W., and Grigsby, L. L. (1989)
Simulation of AC spacecraft power systems.
IEEE Transactions on Industrial Electronics, **36**, 3 (Aug. 1989), 398–402.

[2] Nelms, R. M., and Grigsby, L. L. (1989)
Simulation of DC spacecraft power systems.
IEEE Transactions on Aerospace and Electronic Systems, **25**, 1 (Jan. 1989), 90–956.

[3] Billerbeck, W., and Lewis, G., Jr. (2001)
Spacecraft power system studies using Pspice.
In *Proceedings of the 36th Intersociety Energy Conversion Engineering Conference, Vol. 1*, 2001, 1–18.

[4] Colombo, G., Grasselli, U., Deluca, A., and Spizzichino, A. (1997)
Satellite power system simulation.
Acta Astronautica, **40**, 1 (1997), 41–49.

[5] Cho, B. H., and Lee, F. C. Y. (1988)
Modeling and analysis of spacecraft power systems.
IEEE Transactions on Power Electronics, **3**, 1 (Jan. 1988), 44–54.

[6] Lee, J. R., Cho, B. H., Kim, S. J., and Lee, F. C. (1988)
Modeling and simulation of spacecraft power systems.
IEEE Transactions on Aerospace and Electronic Systems, **24**, 3 (May 1988), 295–304.

[7] Capel, A., Ferrante, J., Cornett, J., and Leblanc, P. (1982)
Power system simulation for low orbit spacecraft: The EBLOS computer program.
In *Proceedings of IEEE Power Electroncs Specialist Conference*, 1982, 272–285.

[8] Dougal, R. A., Brice, C. W., Pettus, R. O., Cokkinides, G., and Meliopoulos, A. P. S. (1998)
Virtual prototyping of PCIM systems—The virtual test bed.
In *Proceedings of PCIM/HFPC '98 Conference*, Santa Clara, CA, Nov. 1998, 226–234.

[9] Meliopoulos, A. P. S., Cokkinides, G., Beker, B., and Dougal, R. (2000)
A new tool for visualization and animation of power component and system operation.
In *Proceedings of the 33rd Hawaii International Conference on System Sciences*, Jan. 2000.

[10] *VHDL Analog and Mixed-Signal Extensions*, IEEE Standards 1076.1-1999, Mar. 1999.

[11] McKay, W., Monti, A., Santi, E., and Dougal, R. (2001)
A co-simulation approach for ACSL-based models.
Presented at the Huntsville Simulation Conference, Huntsville, AL, Oct. 3–4, 2001.

[12] Dougal, R., Lovett, T., Monti, A., and Santi, E. (2001)
A multilanguage environment for interactive simulation and development of controls for power electronics.
Presented at the IEEE Power Electronics Specialists Conference, Vancouver, Canada, June 17–22, 2001.

[13] Dmitriev-Zdorov, V., Dougal, R. A., Merejin, N., Popov, V., and Solodovnik, E. (2001)
Hardware in the loop simulation of energy systems in the VTB environment.
Presented at the 5th IASTED International Conference Power and Energy Systems (PES 2001), Tampa, FL, Nov. 19–22, 2001.

[14] Calahan, D. A. (1972)
Computer-aided network design, (rev. ed.).
New York: McGraw-Hill, 1972.

[15] Prince, M. B. (1955)
Silicon solar energy converters.
Journal of Applied Physics, **26** (May 1955), 534–540.

[16] Rappaport, P., Loferski, J. J., and Linder, E. G. (1956)
The electron-voltaic effect in germanium and silicon p-n junctions.
RCA Review, **17** (1956), 100–128.

[17] Loferski, J. J. (1956)
Theoretical considerations governing the choice of the optimum semiconductor for photovoltaic solar energy conversion.
Journal of Applied Physics, **27** (1956), 777–784.

[18] Rappaport, P. (1959)
The photovoltaic effect and its utilization.
RCA Review, **20** (Sept. 1959), 373–397.

[19] Tringe, J., Merrill, J., and Reinhart, K. (2000)
Developments in thin-film photovoltaics for space.
In *Proceedings of the Twenty-Eighth IEEE Photovoltaic Specialists Conference*, Anchorage, AK, Sept. 15–22, 2000, 1242–1245.

[20] Liu, S., and Dougal, R. A. (2002)
Dynamic multi-physics model for solar array.
IEEE Transactions on Energy Conversion, **17**, 2 (June 2002), 285–294.

[21] Carpenter, B., and Lyons, J. (2001)
Lightweight flexible solar array experiment.
NASA/GSFC EO-1 technology validation report, Aug. 8, 2001, (http://ldcm.usgs.gov/eo-1forum/Validation_Reports/LFSA.pdf).

[22] Wu, B., and White, R. E. (2000)
Self-discharge model of a nickel-hydrogen cell.
Journal of the Electrochemical Society, **147**, 3 (2000), 902–909.

[23] Wu, B., and White, R. E. (2001)
Modeling of a nickel-hydrogen cell, phase reaction in the nickel active material.
Journal of Electrochemical Society, **148**, 6 (2001), 595–609.

[24] Jain, M., Elmore, A. L., Mathews, M. A., and Weidner, J. W. (1998)
Thermodynamic consideration of the reversible potential for the nickel electrode.
Electrochemica Acta, **43**, 18 (1998), 2649–2660.

[25] Liu, S., Dougal, R., Weidner, J., and Gao, L. (2003)
Dynamic model of nickel hydrogen battery—The virtual test bed implementation.
In *Proceedings of IASTED International Conference on Modeling and Simulation, Vol. 1*, Palm Springs, CA, Feb. 2003, 128–136.

[26] Gao, L., Liu, S., and Dougal, R. (2002)
Dynamic lithium-ion battery model for system simulation.
IEEE Transactions on Components and Packaging, **25**, 3 (Sept. 2002), 495–505.

[27] Middlebrook, R. D., and Kimble, S. G. (1976)
Design of the HEAO main bus shunt regulator.
IEEE Transactions on Aerospace and Electronic Systems, **12**, 2 (Mar. 1976), 162–172.

[28] Kuwajima, S., Sato, T., Tsuya, N., Kobayashi, M., Okamura, T., and Honda, Y. (1988)
Digital sequential shunt regulator for solar power conditioning of engineering test satellite (ETS-V).
In *Record of 19th Annual IEEE Power Electronics Specialists Conference, Vol. 2*, 1988, 619–625.

[29] Barry, R. K. (1996)
Conversion from full array shunt to partial shunt topology for two small explorer-class, near-Earth orbiting scientific satellites.
In *Proceedings of the 31st Intersociety Energy Conversion Engineering Conference, Vol. 1*, 1996, 525–528.

[30] Panneton, P., Dakermanji, G., Temkin, D., and Jenkins, J. (2000)
The preliminary design of the comet nucleus tour spacecraft power system.
In *Proceedings of the 35th Intersociety Energy Conversion Engineering Conference, Vol. 1*, 2000, 214–220.

[31] Zhang, S. S., Xu, K., and Jow, T. R. (2003)
The low temperature performance of Li-ion batteries.
Journal of Power Sources, **115**, 1 (Mar. 2003), 137–140.

Zhenhua Jiang (S'01) received the B.Sc. and M.Sc. degrees both in electrical engineering from Huazhong University of Science and Technology, Wuhan, China, in 1997 and 2000, respectively.

He is currently working as a research assistant towards the Ph.D degree in electrical engineering at the University of South Carolina, Columbia. His primary areas of interest are application of power electronics, renewable energy systems, controls, and modeling and simulation of interdisciplinary systems.

Shengyi Liu (S'94—M'96—SM'02) received the B.Sc. in 1982 and the M.Sc. in 1985 from Tsinghua University, Beijing, China, and the Ph. D. in 1995 in electrical engineering, from the University of South Carolina, Columbia.

Prior to joining the Department of Electrical Engineering as a research professor at the University of South Carolina, he was Senior Research and Development Engineer from 1995 to 1999 at InnerLogic, Inc. Research interests include solar and wind energy generation and energy efficiency, application and control study of advanced power sources and systems, modeling and simulation of interdisciplinary systems. His interests also include modeling, design and applications of physical electronics-based devices, power semiconductor devices and converters.

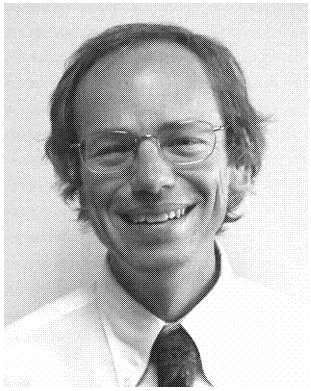

Roger A. Dougal (S'74—M'79—SM'94) earned the Ph.D. degree in electrical engineering at Texas Tech University, Lubbock in 1983.

He joined the faculty in 1983 at the University of South Carolina where he is now the director of the Virtual Test Bed project, which is developing an advanced simulation and virtual prototyping environment for multidisciplinary dynamic systems. Dr. Dougal has received the Samuel Litman Distinguished Professor of Engineering award, and has been honored as a Carolina Research Professor.